Extreme Mechanics Letters 70 (2024) 102183

Contents lists available at ScienceDirect

Extreme Mechanics Letters

journal homepage: www.elsevier.com/locate/eml

Quantized energy absorption of sandwiched origami ring

Bowen Tan, Ke Liu *

Department of Advanced Manufacturing and Robotics, Peking University, Beijing 100871, China

ARTICLE INFO

Keywords:
Origami core
Sandwich plate
Quasi-static
Energy absorption

ABSTRACT

Origami cores are increasingly recognized as effective structures for energy absorption in sandwich plates. However, as most origami sandwich cores are made of tessellations of orthotropic unit cells, their free edges may hinder the formation of plastic hinges and reduce energy absorption capacity. To eliminate such free edges, in this work, by trimming the popular Miura-ori unit cells to form ring-shaped loops, we create a new origami sandwich plate with improved energy absorption efficiency. We study the energy absorption characteristics of these origami ring cores through a combination of theory, numerical simulations, and experiments. Both simulations and experiments verify that the origami ring cores possess quantized energy absorption capacity, related to the number of additional plastic hinges derived from strong local buckling of origami creases. We develop a theoretical model that effectively captures the formation of plastic hinges and predicts their absorbed energy. In summary, the origami ring cores present a novel and promising sandwich plate design approach, characterized by quantized energy absorption performance. This innovation holds significant potential for diverse engineering applications across sectors such as the aeronautic and marine industries and infrastructure development.

1. Introduction

Sandwich plates are lightweight structures with an extraordinary stiffness-to-weight ratio. Owing to their excellent properties [1–6], they have found extensive and diverse applications in aerospace engineering, automotive, and marine industries[7–9]. The sandwich core determines the sandwich plates' mechanical properties, thus affecting its application performance [10]. Therefore, core structures are continuously being developed by researchers and engineers, such as composite foam [11], metallic foam [12], honeycomb [13], corrugated panel [14], lattice [15], and metamaterials [16]. Composite cores are usually made of PVC or PMI foams [17–19] that have advantages in low density [20], isotropy [21], and an ideal yield plateau [22]. Metallic foam cores, e.g., aluminum foam, have the property of isotropy [23], high strength [24], and great resistance to penetration [25]. Honeycomb cores are superior in the out-of-plane strength [26,27]. Corrugated cores possess a strong in-plane strength [28,29]. Lattice cores have advanced thermal insulation and vibration isolation properties [30–32]. Some metamaterial cores have a negative Poisson's ratio [33–35].

In addition to the conventional core structures, foldcores are developed as a novel alternative with attractive properties [36]. Foldcores are made from planar sheets by folding along specific origami patterns [37], which makes the fabrication process simple and straightforward [38,39]. The folding process is highly related to the flat-foldability and rigid-foldability of the origami patterns [40–47]. Proper origami patterns can increase energy absorption and reduce peak force [48]. Ma et al. [49,50] proposed a novel origami pattern inducing a complete diamond mode with much higher energy absorption efficiency than traditional deformation. Then, Wang and Zhou [51] analyzed the effect of manufacturing imperfection on the complete diamond mode. Besides, Kite-shape [52], trapezoid [53], Yoshimura [54], and Tachi-Miura Polyhedron [55] patterns also showed a good improvement in energy absorption capacity, and the quasi-static compression is commonly used to test the origami structures [56].

Among the many foldcores, the most well-known and studied origami pattern is the Miura-ori [57–60] and its derivatives [61,62]. Zhou et al. [63] presented a parametric study on Miura-based foldcores and found improved shear and bending deformation performance. Lv et al. [64] analyzed the quasi-static out-of-plane compression behavior of the Miura-ori sheet and found that the mean force is almost constant with different side lengths and linearly proportional to the square of the thickness. Shi et al. [65] proposed a VAM-based equivalent model to analyze the Miura-based core's global and local buckling behavior. Gattas et al. [66] demonstrated the Miura-based core's moving hinge line failure mode and realized high, uniform reaction stress. Ma et al. [67] designed a graded Miura-based structure, achieving a graded

* Corresponding author.
E-mail address: liuke@pku.edu.cn (K. Liu).

https://doi.org/10.1016/j.eml.2024.102183
Received 28 January 2024; Received in revised form 9 June 2024; Accepted 13 June 2024
Available online 14 June 2024

stiffness property and intrinsic self-locking. Li et al. [68] combined the stacked Miura-ori and the rhombic honeycomb structure, realizing a two-stage programmable compressive strength. However, the current Miura-ori patterns have many free edges that contribute little to energy absorption. Therefore, if the free edges can be closed, the overall energy absorption efficiency of the Miura foldcore sandwich plate may be improved.

This paper studies a Miura-ring core for light weight and improved energy absorption efficiency by enclosing the free edges of Miura-ori to create ring-like structures. The geometry of the Miura-ring sandwich plates is presented in Section 2. An analytical model for the quasi-static compression is established in Section 3. Section 4 gives details about the quasi-static experiments and finite element simulation setups. The results and discussions about the energy-absorbing properties and parametric studies are demonstrated in Section 5. Finally, a conclusion is given in Section 6.

2. Miura-ring sandwich plates

An example of a 3×2 standard Miura-ori core with 12 free edges is shown in Fig. 1(a). As a sandwich structure, the free edges are unconstrained edges of the cores, which means none of those edges is connected to another unit cell or the face sheets. To close the free edges, a Miura-ring unit cell is designed by trimming a Miura-ori unit cell along a central angle of η, as shown in Fig. 1(b). Then, connecting the Miura-ring unit cells in the circumferential direction forms a Miura-ring core, as shown in Fig. 1(c). A sandwich plate is formed by bonding the Miura-ring core or its tessellation to face sheets, as shown in Fig. 1(d). The Miura-ring cores are modularly placed, and do not connect to each other in the sandwich plate.

The basic angular relationship of sector angle α and dihedral angle γ, θ is the same as the Miura-ori core:

$$h = a\sin\alpha\sin\theta \tag{1}$$

$$\gamma = 2\arcsin\frac{\cos\theta}{\sqrt{1-\sin^2\theta\sin^2\alpha}} \tag{2}$$

The central angle of η is defined by the number of unit cells N in the origami ring

$$\eta = \frac{2\pi}{N} \tag{3}$$

Meanwhile, trimming the Miura-ori unit cell generates trapezoidal facets and four new geometrical parameters, i.e., three side lengths b_1, b_2 and a_2 (Fig. 1(b)), and one dihedral angle γ_2. Those parameters can be calculated from the following equations

$$b_1 = b - \frac{\sin\frac{\eta}{2} \bullet \sqrt{a^2-h^2}}{\sin(\frac{\eta}{2}+\arccos\frac{\cos\alpha}{\sqrt{1-\sin^2\theta\sin^2\alpha}})} \tag{4}$$

$$b_2 = b - 2\frac{\sin\frac{\eta}{2} \bullet \sqrt{a^2-h^2}}{\sin(\frac{\eta}{2}+\arccos\frac{\cos\alpha}{\sqrt{1-\sin^2\theta\sin^2\alpha}})} \tag{5}$$

$$a_2 = \sqrt{(b-b_1)^2 + a^2 - 2a(b-b_1)\cos\alpha} \tag{6}$$

$$\gamma_2 = 2\arctan\frac{a_2\tan\left(\frac{\eta}{2}+\arctan\frac{h\tan\gamma}{a}\right)}{h} \tag{7}$$

For the case of a = b and N = 6, the dimensions of the trapezoidal facets compared to the original are plotted in Fig. 2. Here, S is defined by the total surface area of a unit cell, and the subscripts R, M indicate the Miura-ring and the Miura-ori. It can be seen that the surface ratio S_R/S_M is identical to the side length ratio b_1/b, and the dihedral angle γ_2 is larger than the original, while the others are smaller. Notably, those ratios coherently decrease with the increase of the dihedral angle γ and increase as the sector α, as shown in Fig. 2(a and b). Meanwhile, the opposite tendency of the side length ratios and the dihedral angle ratio is observed for the number of unit cells N, as shown in Fig. 2(c). The side length ratio a_2/a is approximately a constant of nine-tenths at variant γ and N, and that of b_1/b approximates two-thirds at variant γ. As a result, the Miura-ring core saves more than one-third of the materials of a Miura-ori core.

3. Analytical model for energy absorption

When the Miura-ring core is crushed, the deformation is a progressive process, as shown in Fig. 3(a). The mountain and valley edges buckle in two opposite directions, forming four moving hinge lines on each edge (red lines). Following the edge buckling, the facets bend and generate several stationary plastic creases (black lines). Moreover, more surface bending deformation occurs when the deformed edges are in contact with the face sheet.

A basic folding element is extracted from the crushed Miura-ring core, as shown in Fig. 3(b). The geometry of the basic folding element is composed of two oblique facets of an angle θ and a side length of 2 H. The upper and lower ends of the basic folding element are constrained. The upper point is set to be able to move along the vertical direction, and the lower is considered a fixed point. When the basic folding element is compressed vertically by a force (P), its component along the mountain fold, P_1, is generated. The mountain edge is forced into two moving hinge lines and rolling to new positions. At the same time, the facets bend into stationary plastic creases.

Wierzbicki and Abramowicz [69] established a kinematic model to analyze such a progressive deformation and proposed the *Super Folding Element Method* for metal tubes. The original *Super Folding Element* assumes straight cell walls and compression along the vertical direction. Hence, the direction of the loads is the same as the direction of the

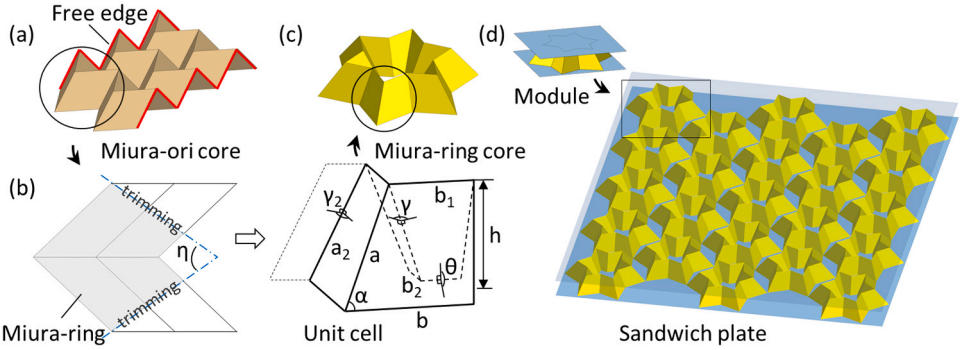

Fig. 1. (a) 3×2 Miura-ori core with free edges. (b) A Miura-ring unit cell from trimming the Miura-ori unit cell. (c) Miura-ring core composed of 6-unit cells with closed edges. (d) Sandwich plate with a tessellation of the Miura-ring sandwich module.

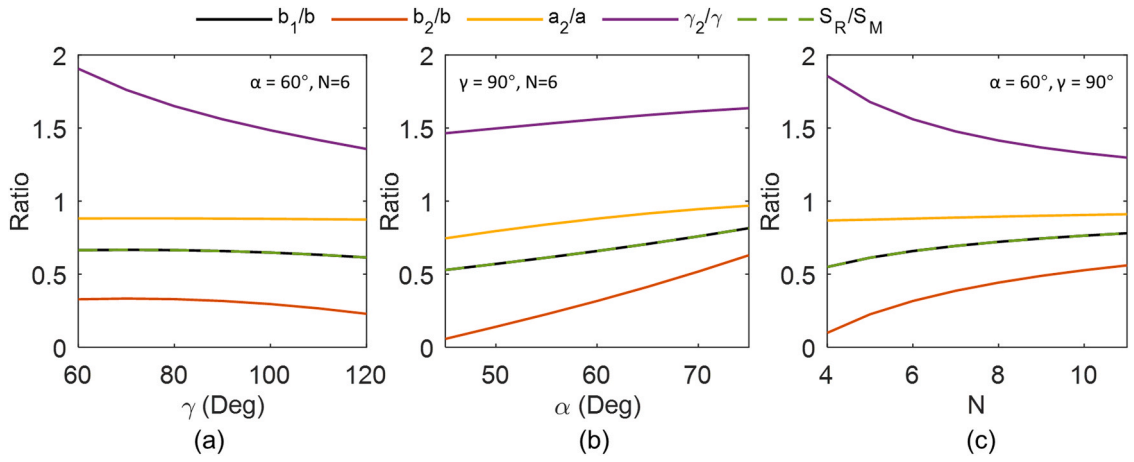

Fig. 2. Trimming ratio of the Miura-ring core from the Miura-ori core versus (a) dihedral angle γ, (b) sector α, and (c) number of unit cells N.

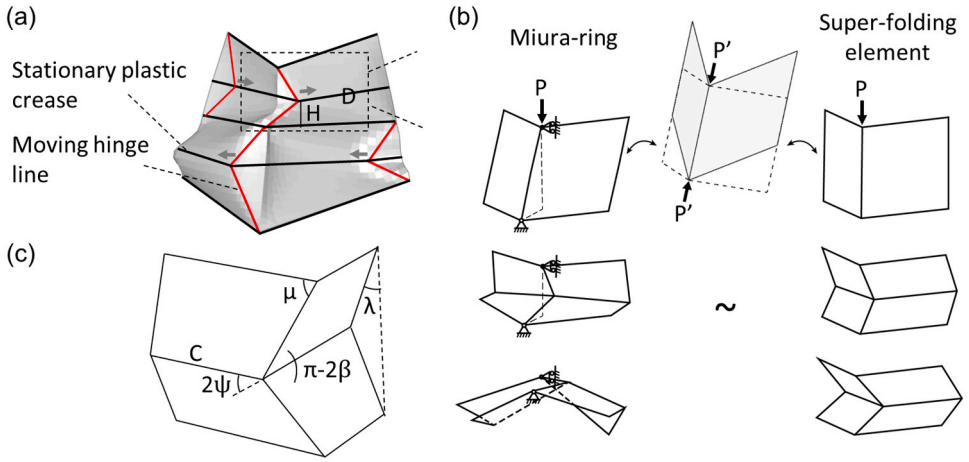

Fig. 3. Folding mechanism of Miura-ring unit cell. (a) Deformation of a Miura-ring unit cell. (b) One of the basic folding elements. (c) *Super folding element* [69].

straight cell walls. Similarly, the in-plane component force P_1 of the Miura-ring cell is in the same direction as the oblique facets and rotating as the compression of the basic folding element. Therefore, the deformation of the Miura-ring cell is similar to the straight cell wall, and the *Super Folding Element Method* is applicable as an approximate model for the post-buckling behavior of the Miura-ring cells. However, the oblique facets lead to an inadequate development of the *Super Folding Element*. For example, the super folding element is only half-folded when the top side is compressed to the same level as the bottom side, as shown in Fig. 3(b).

For a *Super Folding Element* that is full-folded, as shown in Fig. 3(c), its deformation energy is calculated as [69]

$$2HP_m = M_0\left[16I_1\frac{\rho H}{t} + 2\pi C + 4I_3\frac{H^2}{\rho}\right] \tag{8}$$

where the plastic bending moment $M_0 = \sigma_0 t^2/4$, and $\sigma_0 = \sqrt{\sigma_y\sigma_u/(1+n')}$. σ_y, σ_u represent the yield and ultimate strength, n' is the hardening exponent. C is the length of the stationary hinge line. H is the sub-wavelength of the super folding element, ρ is the normal radius of curvature of the moving hinge line. I_1 and I_3 are integration constants of folding angles. $I_1(\psi_0) = \frac{\pi}{(\pi-2\psi_0)tg\psi_0}\int_0^{\pi/2}\cos\alpha\left\{\sin\psi_0\sin\left(\frac{\pi-2\psi_0}{\pi}\right)\beta + \cos\psi_0\left[1-\cos\left(\frac{\pi-2\psi_0}{\pi}\right)\beta\right]\right\}$, and $I_3(\psi_0) = \frac{1}{tg\psi_0}\int_0^{\pi/2}\frac{\cos\lambda}{\sin\mu}$.

The deformation of the Miura-ring core is a collection of the super folding elements. During the deformation, the energy dissipation includes membrane energy and bending energy. The membrane energy E_1 comes from the circumferential extension of the surface on the moving hinge line. The bending energy is composed of the folding E_2 of the stationary plastic creases and the moving hinge lines E_3. Moreover, the flattening of the existing fold lines E_4 (side lengths b, b_1, b_2, a, a_2 (Fig. 1 (b))) is also considered in our model. Following the *Super Folding Element Method* [69–71], an analytical model can be established as

$$P_m h\kappa = N[mE_1 + \hat{n}E_2 + mE_3] + NE_4 \tag{9}$$

where P_m is the mean force, h is the height of the Miura-ring core, κ is the effective crushing coefficient of 0.75 [72], m and $\hat{n}$ are the number of super folding elements and stationary plastic creases, respectively. The symbol N represents the number of the unit cells in a ring.

The membrane energy E_1 is determined by [69]

$$E_1 = \frac{16M_0H\rho I_1}{t} \tag{10}$$

The stationary hinge line D is perpendicular to the mountain edge. The total length of the stationary hinge lines at the same height is a constant as $C = 4b/\sin\alpha$, and we call them a global lateral crease. The stationary hinge lines tend to fold with an angle of π. Therefore, the bending energy of a global lateral crease E_2 is given by

$$E_2 = \pi M_0 C \tag{11}$$

The bending energy of the moving hinge lines E_3 is determined by [69]

$$E_3 = \frac{4M_0 I_3 H^2}{\rho} \tag{12}$$

The flattening energy of the existing folds E_4 is given by:

$$E_4 = 2M_0[a(\pi-\gamma) + a_2(\pi-\gamma_2) + b\theta + 2b_1\theta + b_2\theta] \tag{13}$$

Usually, the number of super folding elements m is determined by the structural height and the sub-wavelength H, i.e., per length of 2 H generates a super folding element [69–71]. However, the oblique facets hinder the development of the super folding elements that only form two on each mountain and valley edge, i.e., eight super folding elements on a Miura-ring unit cell (m = 8). The rest of the side lengths induce different stationary plastic creases. Thus, the stationary hinge line piles up, but the quantity $\hat{n}$ appears with some uncertainty.

Because the number of the super folding elements is determined, the energy of the super folding elements can be obtained. To simplify calculations, the parameters H, ρ are determined by minimizing the force of half-folded super folding elements (Eq. 8) with respect to H and ρ. For $2\psi_0 = \pi/2$, we get $I_1 = 0.415$, $I_3 = 0.762$, and

$$H = 0.989t^{1/3}D^{2/3},\ \rho = 0.52t^{2/3}D^{1/3} \tag{14}$$

where D is selected as an equivalent value, $D = (b+b_1)/2\sin\alpha$. The mean force P_m for the Miura-ring core is

$$P_m h\kappa = NM_0\left(\frac{53.2H\rho}{t} + \frac{24.4H^2}{\rho} + a\pi + 2a_2(\pi-\gamma_2) + 8b_1\theta\right) + \hat{n} \bullet N\pi M_0 C. \tag{15}$$

Here, the only undetermined parameter is the number of global lateral creases $\hat{n}$, which depends on the geometry and leads to a quantized energy absorption. The determination about $\hat{n}$ is discussed in Section 5.

4. Experiment and simulation

This section introduces the fabrication procedure of the Miura-ring core and the quasi-static experimental setup for the out-of-plane compression. The details of the finite element model according to the experiment are also explained.

4.1. Fabrication and experiment

The Miura-ring sandwich plates have two rigid face sheets and a weak Miura-ring core. The dimensions of the Miura-ring cores are selected as a = b = 15, 19, 23, 24, 27, 39 mm, γ = 90°, and α = 60°. We select 1060 aluminum sheets of 1 mm and 0.2 mm thickness to produce the face sheets and the Miura-ring core, respectively. Due to the self-locking properties, two facets were halved, as shown in Fig. 4(a). Then, the crease pattern of the Miura-ring core is cut from an aluminum sheet. The sheet is shaped based on the geometrical relationships described in Section 2 by setting the folding angle γ to 180°.

Next, a Miura-ring core is fabricated by folding the crease pattern. To reduce the unexpected deformation, we divided the forming process into three steps (γ equals 150°, 120°, and 90°). Molds are designed to help form the Miura-ring core geometry, as shown in Fig. 4(a). By adjusting γ to 150°, 120°, and 90°, the shape of the molds is obtained. The molds were made on a 3D printer using ABS resin. Due to the rotational symmetry of the Miura-ring, the molds of γ equaling 150° and 120° were only fabricated one and a half unit cells. The sheet was stamped one by one by the male and female molds. Finally, a complete Miura-ring mold was used to stamp the aluminum sheet to the designated Miura-ring core. Adhesive films (Ergo 5996, Kisling AG) were used to close the open loop and bond the face sheets.

The quasi-static out-of-plane compression test for the sandwich plates was conducted using an MTS machine E44.305. The cross-head speed was set as 10 mm/min, and the corresponding displacement δ and force F were recorded at 0.1 s intervals. To observe the deformation and the mean force, two groups of specimens were tested with compression distances of 0.3 h and 0.75 h. The mean force is defined as

$$F_{mean} = \frac{\int F(\delta)d\delta}{\delta_u}, \tag{16}$$

where δ_u is the total compression distance.

For conducting numerical analysis, a 1060 aluminum sheet tensile specimen is tested using the same universal testing machine. The material properties were obtained as: density $\boldsymbol{\rho} = 2700\ kg/m^3$, Young's modulus $E = 69$ GPa, Poisson's ratio $\upsilon = 0.3$, yield stress $\sigma_y = 106$ MPa, and ultimate stress $\sigma_u = 149.6$ MPa. The Voce material model was used to fit the true stress-strain relationship as

$$\sigma = A - Be^{-C\varepsilon}. \tag{17}$$

The coefficients are fitted as: A = 149.6MPa, B = 118.8 MPa, and C = 197.4.

4.2. Finite element model

The numerical simulation of the sandwich plates was performed with commercial software ANSYS/LS-DYNA. The finite elements were established as the test specimens, as shown in Fig. 5. Both the face sheets and the core were meshed by a 4-node Belytschko-Tsay shell element with reduced integration. The shell elements were divided into five integration points in the thickness direction. The mesh size was selected as 1 after the mesh convergence study. A piecewise linear plasticity material model was adopted for the core of 1060 aluminum, and the table of stress-strain curve was obtained by Eq. (17). The strain rate effect was not considered. As the

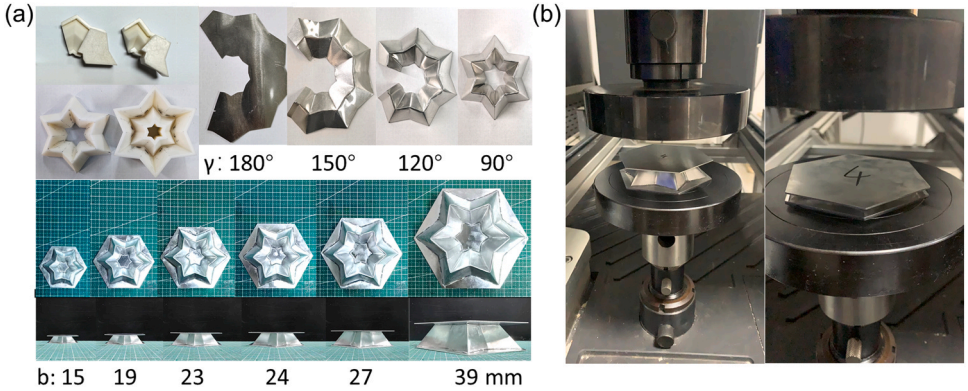

Fig. 4. Fabrication and experiment setups of the Miura-ring sandwich plates. (a) ABS resin molds and partially folded samples with the dihedral angle γ equal to 150°, 120°, and 90°. (b) The quasi-static out-of-plane compression test for the sandwich plates.

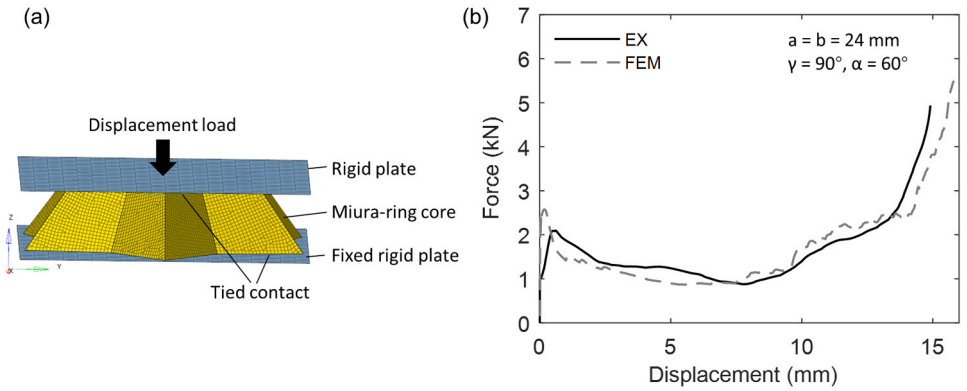

Fig. 5. (a) FE model of 6-unit cells Miura-ring sandwich plates. (b) Validation of the numerical simulation by load-displacement curve.

face sheets are almost non-deforming, they were set as rigid plates. The lower face sheet was fixed in all directions. The upper face sheet was fixed in five directions except for the vertical direction. A constant compression speed of 1 m/s was applied to the upper face sheet [68]. The upper and bottom edges of the core were connected to the face sheets by tied contact, respectively [38]. A surface-to-surface contact was also defined between them with a friction coefficient of 0.25. Furthermore, a self-contact with a friction coefficient of 0.25 was defined on the core [61]. During the numerical simulation, the ratio of kinetic to internal energy was limited to be lower than 5 % [66].

The load-displacement curve of the Miura-ring core by experiment and numerical simulation are compared in Fig. 5(b), and the results show a good overall agreement, especially in the large deformation range. As both physical and numerical models revealed, the crushing resistance increases drastically in the elastic stage. The difference in the elastic stage between the two models is likely due to the imperfect geometry and boundary condition. After the elastic stage, the load drops slightly during the subsequent plateau stage, and the super folding elements form progressively. Due to the deformed super folding elements (non-fully folded) being in contact with the face sheets again, the loads rise again, leading to a densification stage.

5. Results and discussion

This section compares the analytical model, FE simulation, and experiments. Parametric studies are conducted to explore the effect of geometry on the number of lateral creases $\hat{n}$. Two types of sandwich plates with different development methods are investigated. Finally, the difference between a Miura-ori core and a Miura-ring core is analyzed.

5.1. Effect of geometric parameters

As Lv et al. [57] mentioned, Miura-ori plates have a constant mean force with different side lengths, and the Miura-ring core also presents a constant mean force from the theoretical analysis, as shown in Fig. 6(a). However, the uncertainty of the crease generation number $\hat{n}$ makes the mean forces not monotonic. Notably, the fluctuation amplitude is nearly the energy of one global lateral crease, as $\hat{n}$ being mostly integers. The case of $\hat{n} = 0.5$ means that one global crease is only half-folded due to the compression distance not allowing for fully developed super folding

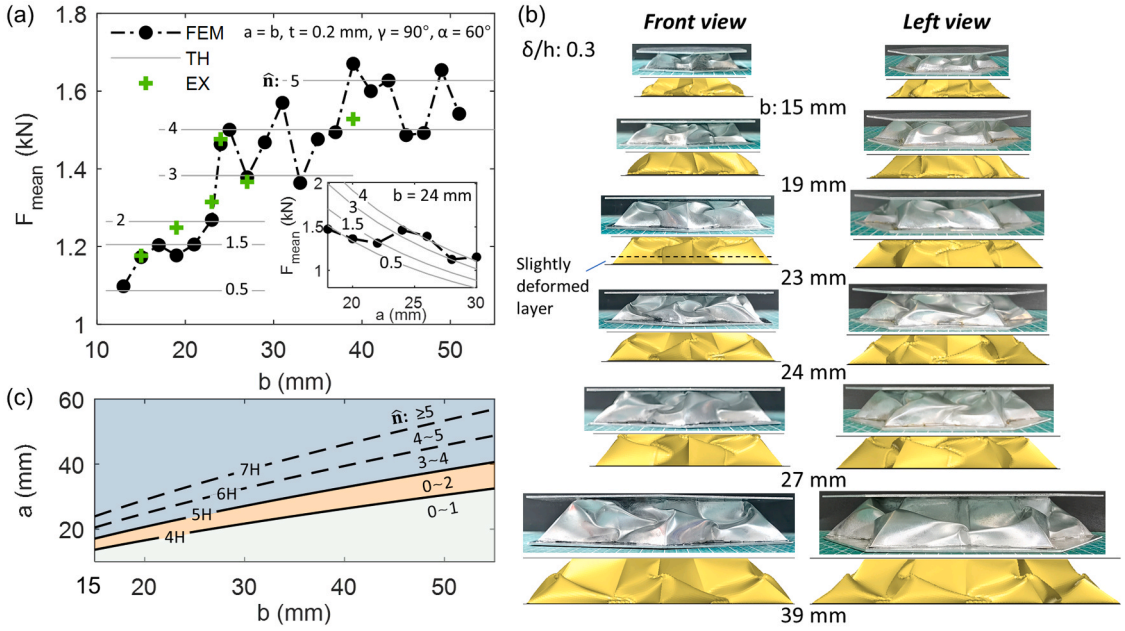

Fig. 6. The effect of side lengths on Miura-ring sandwich plates. (a) Numerical, theoretical, and experimental results of mean force under a max compression distance of 0.75 h; the inset shows the effect of the side length of the mountain edge under a fixed side length b. (b) Numerical and experimental results of deformation at the compression distance of 0.3 h. (c) Identification of the number of creases versus side lengths a, b (H is the halfwave length of a super folding element). The silver ones are experimental, and the golden ones are numerical.

element. Such a situation is because the folding of a layer of super folding elements must be completed before the next one starts to fold, so the last one may not have enough compression distance. Moreover, as shown in the inset of Fig. 6(a), the mean force in the theoretical model decreases as the increase of the side length of the mountain edge, but $\hat{n}$ tends to increase to balance out the lost of energy. Therefore, the mean force is relatively stable versus side length.

Combining the deformation results, as shown in Fig. 6(b), we can observe that the numerical results are in qualitatively good agreement with the experiments. Due to the same boundary conditions, the deformation mode of each unit cell is similar in the numerical simulations. Although the fabrication errors make some differences in the experiments, the folding states of the Miura-ring core still exhibit an axisymmetric trend. The sudden dropping of $\hat{n}$ is observed both in FE analyses and experiments. For b = 23 and 27 mm, the bottom layer is only deformed slightly, which decreases the energy and $\hat{n}$. The size of the upper super folding element is generally smaller than the bottom super folding element. The experiment result of b = 39 mm also shows the same situation, so that $\hat{n}$ decreases by one. For b = 23 and 24 mm, their dimension is nearly the same, but $\hat{n}$ deviates nearly by 2. The slightly increased width leaves just enough room to accommodate additional full development of super folding elements.

The number of creases $\hat{n}$ is related to the side lengths a, b and the dimension of super folding elements (halfwave length H), which is summarized in Eq. 6(c) and Eq. 18. When a < 4H, the side length is not enough to form two super folding elements so that only one element is formed. The plastic creases are generated in the middle of the facets with $\hat{n} = \theta/\frac{\pi}{2}$. When 4H < a < 5H, the side length is just enough to form two super folding elements, so two plastic creases are generated with $\hat{n} = 2\theta/\frac{\pi}{2}$. The case of b = 23 mm is near this region, whereas the case of b = 24 mm is in the next region. When a ≥ 5H, it still forms two super folding elements, but the rest of the side length and facets are transformed into $\hat{n}$, and $\hat{n}$ increases by one per additional H.

$$\hat{n} = \begin{cases} \theta/\frac{\pi}{2}, & a < 4H \\ 2\theta/\frac{\pi}{2}, & 4H < a < 5H \\ \left[\frac{a-2H}{H}\right], & a \geq 5H \end{cases} \tag{18}$$

The effect of dihedral angle γ, sector α, and number of unit cells N on $\hat{n}$ is shown in Fig. 7. Here, $\hat{n}$ is identified by a comparison of theoretical values and numerical simulations (see Fig. 6(a)). Apparently, a decreasing tendency of $\hat{n}$ is achieved as the increase of γ, as shown in Fig. 7(a). Although $\hat{n}$ varies with side lengths, they decrease to 0 at the same time, i.e., $\hat{n}$ of a large side length changing faster. For b = 15 and 19 mm, they have the same $\hat{n}$, while the others are different and keep a stable grade difference. Meanwhile, $\hat{n}$ increases with sector α, but the change of α makes the grade differences unstable, particularly for a large side length, as shown in Fig. 7(b). In addition, the number of unit cells N also affects $\hat{n}$, because a large γ_2 weakens the super folding element, as shown in Fig. 7(c). Then, $\hat{n}$ becomes stable when N is larger than 6.

The effect of wall thickness t on $\hat{n}$ is analyzed by numerical simulations, as shown in Fig. 8. $\hat{n}$ decreases as the wall thickness increases, and the symmetry of deformation is enhanced gradually. When t is less than 0.2 mm, two super folding elements form on the mountain edge. Then, the wall thickness increases the size of the super folding element. The upper super folding element gradually declines and vanishes at t = 0.3 mm. Afterward, due to increased structural strength by wall thickness, the upper part keeps symmetry and extrudes the bottom part to form a super folding element. Finally, when t > 0.5 mm, the deformation of the entire Miura-ring core remains symmetric, and no super folding element is formed.

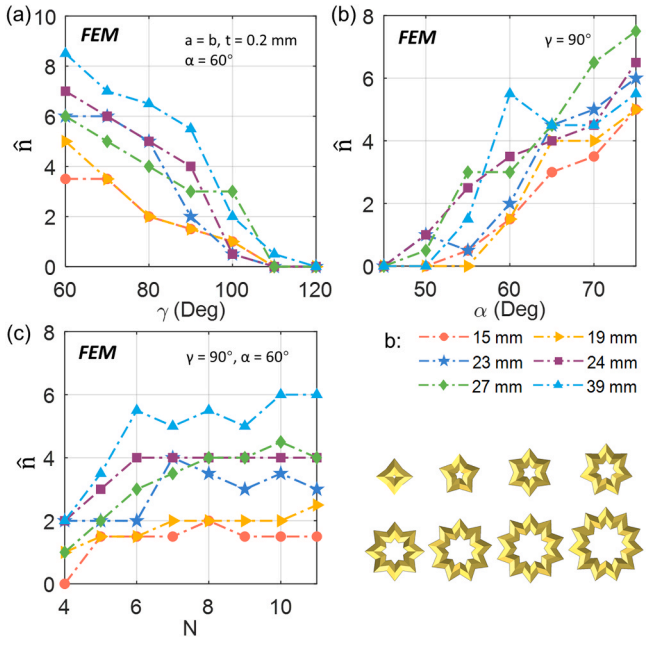

Fig. 7. The effect of (a) dihedral angle γ, (b) sector α, and (c) number of unit cells N on $\hat{n}$ under a max compression distance of 0.75 h.

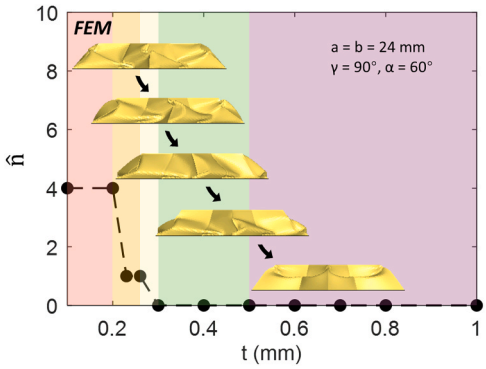

Fig. 8. The effect of wall thickness on deformation modes and $\hat{n}$ of Miura-ring cores.

5.2. *Miura-ring sandwich plate by tessellation*

There are two ways to construct a Miura-ring based sandwich plate: the extension structure (type I) and the tessellation structure (type II), as shown in Fig. 9. The two structures have the same projected area and height. We study the mean force of the two types of structures by numerical simulations. We observe that in general, the mean force of the extension structure is lower than the tessellation structure. Due to the increased side length b of the outer rings of the extension structure, the number of the super folding element $\hat{n}$ decreases rapidly. Owing to the diminishing effect of $\hat{n}$, and the extension structures have very similarmean forces. The interaction action between adjacent rings causes the differences in the mean forces. In constrast, the Miura-ring cores in the tessellation structure are all independent, so they have the same deformation and force. Ultimately, the tessellation structure forms more super folding elements and plastic creases than the extension structure, leading to higher energy absorption.

5.3. *Comparison of Miura-ring and Miura-ori cores*

We performed a comparison through numerical simulations to

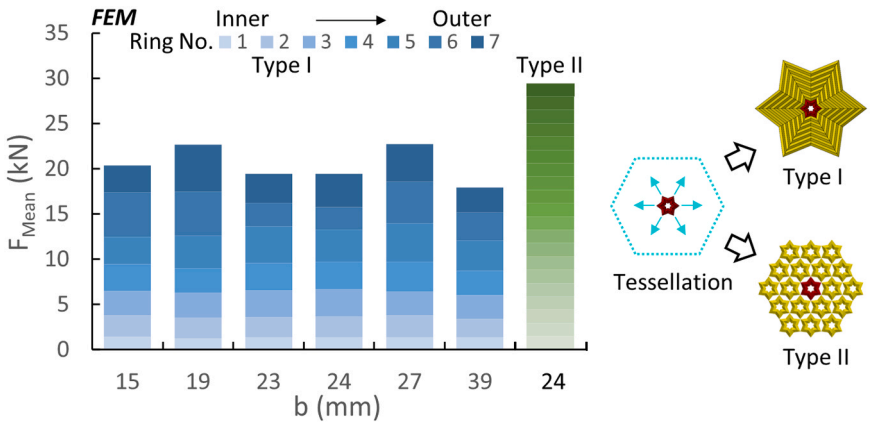

Fig. 9. Tessellating a sandwich plate by Miura-ring cores and comparison of the mean force of each ring. Each color represents a 6-unit cell Miura ring.

investigate the difference between the Miura-ring core and the Miura-ori core withequally sized face sheets, as shown in Fig. 10(a). The Miura-ori unit cell only forms one super folding element on each side. Meanwhile, the Miura-ring unit cell forms two super folding elements on each side and more lateral creases on the facets. The increased deformation compensates for the energy loss of the reduced facet area due to trimming of the Miura-ring unit cell. So, the average compressive stress of the 3×6 Miura-ring core is similar to the 4×4 Miura-ori core, as shown in Fig. 10(b). The average compressive stress is calculated by $\hat{\sigma} = F/A_c$, where A_c denotes the area of the cores projected onto the face sheets. The SEA of each unit cell during compression is shown in Fig. 10(c). Due to the boundary effect, the SEA of the Miura-ori cells with constrained boundaries is similar to the Miura-ring cells. Meanwhile, the Miura-ori unit cells with free edges show decreased energy absorption by nearly 40 %, compared to fully surrounded Miura-ori unit cells.

Considering that the mass of a Miura-ring unit cell is only two-thirds of the Miura-ori unit cell, the specific energy absorption SEA (SEA = energy/mass) increases by 30~63 %, as shown in Fig. 10(c). Notably, as the wall thickness decreases to 0.1 mm, the unit cell of the Miura-ori core also forms two super folding elements on each side. That enables the Miura-ori core to have the same mean force as t = 0.2 mm and increase SEA by 100 %, hence the better performance of the Miura-ori foldcores when t is less than 0.2 mm.

We compared the average force of the two from experimental measurements, as shown in Fig. 10(e). The experimental data for Miura-ori foldcore is from Cheng and Li [73], on the 4×4 Miura-ori sandwich plate, which had the same geometry and material as the numerical simulation. The initial peak force of the Miura-ring unit cell is slightly lower than the Miura-ori unit cell, while the compression stroke is a little higher. The two unit cells have similar energy absorption, but the Miura-ring core saves about 30 % of weight.

Although the Miura-ori is known to be a rigid folding origami, when it is used for sandwich core, its deformation mode becomes a panel deformation due to the fixed boundary constraints on the top and bottom. Meanwhile, the lateral boundaries of the unit cells also affect the deformation. For a 4×4 Miura-ori core, their boundaries are complicated, as some unit cells have left or right free edges, or fully constrained edges. Therefore, the Miura-ori unit cells may form one or two super folding elements during deformation. The energy absorption of each unit cell is compared in Fig. 11. Both the elimination of free boundaries and the increase of super folding elements improve the energy absorption capability of Miura-ori unit cells. The Miura-ring unit cells satisfy the two conditions at the same time, so their energy absorption capability is equal to the highest value of Miura-ori unit cells.

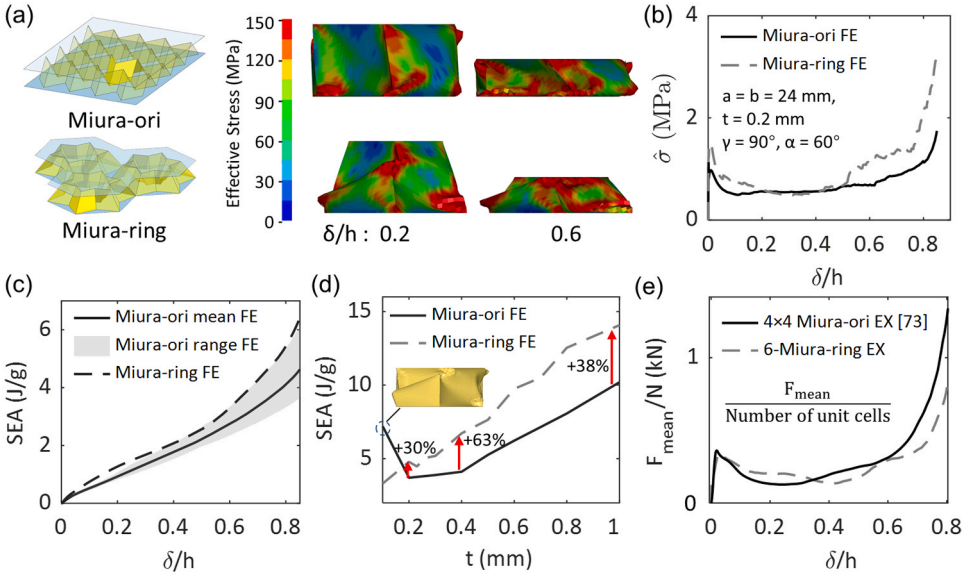

Fig. 10. Comparison between Miura-ori core and Miura-ring core. (a) Deformation modes of one unit cell from a 4×4 Miura-ori pattern and a 3×6 Miura-ring pattern. (b) Average compressive stress on the bottom face sheet. (c) SEA of each unit cell, and shaded envelope delimit maximum and minimum value ranges of different Miura-ori unit cells. (d) SEA versus wall thickness. (e) Average force of a unit cell from experimental measurements of 4×4 Miura-ori [73] and 6-Miura-ring.

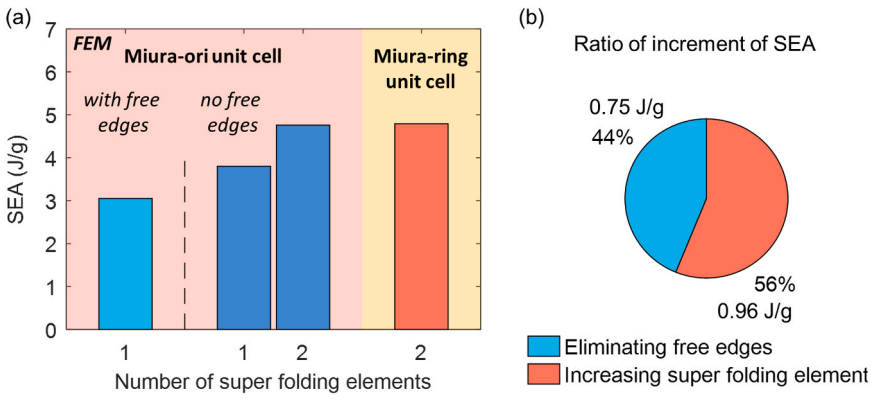

Fig. 11. Effect of free edges and deformation modes on energy absorption capability via FEM. (a) SEA of Miura-ori unit cells on the outside and inside of a tessellation with different types of edges. (b) Ratio of increment of SEA from a Miura-ori unit cells with free edges.

6. Conclusions

This paper investigates a sandwiched Miura-ring core structure with improved energy absorption capability by eliminating free edges. The energy-absorbing performances and deformation modes are analyzed via theoretical, numerical, and experimental approaches. A theoretical model was developed for the quasi-static out-of-plane compression of the Miura-ring core. Quasi-static experiments were conducted to validate the theoretical and numerical results. The Miura-ring unit cell trims the facets of the standard Miura-ori unit cell, leading to trapezoidal facets that accommodate more super folding elements and plastic creases than the conventional Miura-ori. The number of post-buckling lateral creases $\hat{n}$ is nonmonotonic and sensitive to geometrical dimensions. However, $\hat{n}$ generally increases by the side lengths a, b and sector angle α, and decreases by the dihedral angle γ and wall thickness t. The increase in plastic deformation and the decrease in mass enhanced the SEA by more than 30 % compared to the Miura-ori cores.

Our discovery shows that origami ring is an efficient approach for improving the energy absorption of origami cores. In addition, the developed theoretical models and thorough analyses could provide a framework for developing other efficient energy-absorbing foldcore structures.

CRediT authorship contribution statement

Ke Liu: Writing – review & editing, Validation, Supervision, Funding acquisition. **Bowen Tan:** Writing – original draft, Methodology, Investigation, Conceptualization.

Declaration of Competing Interest

The authors declare that they have no known competing financial interests or personal relationships that could have appeared to influence the work reported in this paper.

Data availability

Data will be made available on request.

Acknowledgments

This research is supported by the National Key Research and Development Program of China through grant 2022YFB4701900, and the National Natural Science Foundation of China through grant 12372159. The authors also thank Dr. Xiangxin Dang for helpful discussions during the development of this research.

References

[1] X.R. Liu, X.G. Tian, T.J. Lu, B. Liang, Sandwich plates with functionally graded metallic foam cores subjected to air blast loading, Int J. Mech. Sci. 84 (2014) 61–72.
[2] J.Y. Liu, W.F. Qiao, J.X. Liu, D. Xie, Z.G. Zhou, L. Ma, L.Z. Wu, The compressive responses of glass fiber composite pyramidal truss cores sandwich panel at different temperatures, Compos Part a-Appl. S 73 (2015) 93–100.
[3] Y.J. Xu, N.X. Xu, W.H. Zhang, J.H. Zhu, A multi-layer integrated thermal protection system with C/SiC composite and Ti alloy lattice sandwich, Compos Struct. 230 (2019).
[4] V.T. Le, N. San, Ha, N.S. Goo, Advanced sandwich structures for thermal protection systems in hypersonic vehicles: A review, Compos Part B-Eng. (226 () (2021).
[5] H. Li, X.T. Wang, Z.H. Dai, Y. Xia, S.K. Ha, X.P. Wang, Y.P. Ren, Q.K. Han, H.H. Wu, Magnetic and vibrational amplitude dependences of MRE grid composite sandwich plates, Int J. Mech. Sci. 241 (2023).
[6] Z.K. Guo, C.C. Liu, F.M. Li, Vibration analysis of sandwich plates with lattice truss core, Mech. Adv. Mater. Struc 26 (2019) 424–429.
[7] H. Li, X.T. Wang, X.Y. Hu, J. Xiong, Q.K. Han, X.P. Wang, Z.W. Guan, Vibration and damping study of multifunctional grille composite sandwich plates with an IMAS design approach, Compos Part B-Eng. 223 (2021).
[8] F.M. Li, Z.G. Song, C.C. Sun, Aeroelastic Properties of Sandwich Beam with Pyramidal Lattice Core Considering Geometric Nonlinearity in the Supersonic Airflow, Acta Mech. Solid. Sin. 28 (2015) 639–646.
[9] Y.Q. Wang, H. Wu, F.L. Yang, Q. Wang, An efficient method for vibration and stability analysis of rectangular plates axially moving in fluid, Appl. Math. Mech. -Engl. 42 (2021) 291–308.
[10] L.J. Gibson, M.F. Ashby, Cellular solids: structure and properties, Cambridge University Press, Cambridge, 1999.
[11] W.T. Lv, D. Li, L. Dong, Study on blast resistance of a composite sandwich panel with isotropic foam core with negative Poisson's ratio, Int J. Mech. Sci. 191 (2021).
[12] Y.F. Zhu, Y.G. Sun, Low-velocity impact response of multilayer foam core sandwich panels with composite face sheets, Int J. Mech. Sci. 209 (2021).
[13] W.T. He, S.J. Lu, K. Yi, S.Q. Wang, G.Y. Sun, Z.Q. Hu, Residual flexural properties of CFRP sandwich structures with aluminum honeycomb cores after low-velocity impact, Int J. Mech. Sci. 161 (2019).
[14] B. Hou, Y. Wang, Z.B. Tang, H. Zhao, X.L. Xi, Y.L. Li, The mechanical behaviors of corrugated sandwich panel under quasi-static and dynamic shear-compressive loadings, Int J. Impact Eng. 156 (2021).
[15] K. Wei, Q.D. Yang, B. Ling, X.J. Yang, H.G. Xie, Z.L. Qu, D.N. Fang, Mechanical properties of Invar 36 alloy additively manufactured by selective laser melting, Mat. Sci. Eng. a-Struct. 772 (2020).
[16] X.C. Teng, W. Jiang, X.G. Zhang, D. Han, X.H. Ni, H.H. Xu, J. Hao, T. Guo, Y.F. Wu, Y.M. Xie, X. Ren, A stretchable sandwich panel metamaterial with auxetic rotating-square surface, Int J. Mech. Sci. 251 (2023).
[17] X.T. Huo, Z.C. Jiang, Q.T. Luo, Q. Li, G.Y. Sun, Mechanical characterization and numerical modeling on the yield and fracture behaviors of polymethacrylimide (PMI) foam materials, Int J. Mech. Sci. 218 (2022).
[18] J.Z. Chen, L. Cheng, H.T. Sun, X.M. Yao, C.C. Fu, J.J. Jiang, The influence of pin on the low-velocity impact performance of foam sandwich structure, Int J. Mech. Sci. 244 (2023).
[19] H.S. Lei, K. Yao, W.B. Wen, H. Zhou, D.N. Fang, Experimental and numerical investigation on the crushing behavior of sandwich composite under edgewise compression loading, Compos Part B-Eng. 94 (2016) 34–44.
[20] L. Alonso, A. Solis, High-velocity impact on composite sandwich structures: A theoretical model, Int J. Mech. Sci. 201 (2021).
[21] V.S. Deshpande, N.A. Fleck, Multi-axial yield behaviour of polymer foams, Acta Mater. 49 (2001) 1859–1866.
[22] I. Ivañez, C. Santiuste, E. Barbero, S. Sanchez-Saez, Numerical modelling of foam-cored sandwich plates under high-velocity impact, Compos Struct. 93 (2011) 2392–2399.

[23] X.Y. Zhang, L.Q. Tang, Z.J. Liu, Z.Y. Jiang, Y.P. Liu, Y.D. Wu, Yield properties of closed-cell aluminum foam under triaxial loadings by a 3D Voronoi model, Mech. Mater. 104 (2017) 73–84.
[24] X.T. Huo, H. Liu, Q.T. Luo, G.Y. Sun, Q. Li, On low-velocity impact response of foam-core sandwich panels, Int J. Mech. Sci. 181 (2020).
[25] K. Mohan, T.H. Yip, S. Idapalapati, Z. Chen, Impact response of aluminum foam core sandwich structures, Mat. Sci. Eng. a-Struct. 529 (2011) 94–101.
[26] Z.H. Zhang, S.T. Liu, Z.L. Tang, Comparisons of honeycomb sandwich and foam-filled cylindrical columns under axial crushing loads, Thin Wall Struct. 49 (2011) 1071–1079.
[27] J.F. Zhou, B.F. Ng, N. Han, S.C. Xu, M. Zou, Crashworthiness and optimization of bionic sandwich cores under out-of-plane compression, Int J. Mech. Sci. 246 (2023).
[28] J. Bai, J. Wang, L. Pan, L.X. Lu, G.X. Lu, Quasi-static axial crushing of single wall corrugated paperboard, Compos Struct. 226 (2019).
[29] P.B. Su, B. Han, M. Yang, Z.H. Wei, Z.Y. Zhao, Q.C. Zhang, Q. Zhang, K.K. Qin, T. J. Lu, Axial compressive collapse of ultralight corrugated sandwich cylindrical shells, Mater. Des. 160 (2018) 325–337.
[30] L. Zhang, Y.F. Chen, R.J. He, X.J. Bai, K.Q. Zhang, S.G. Ai, Y.Z. Yang, D.N. Fang, Bending behavior of lightweight C/SiC pyramidal lattice core sandwich panels, Int J. Mech. Sci. 171 (2020).
[31] Z.P. Zhang, Y.W. Wang, W. Zhang, Temperature- and moisture-dependent aeroelastic stability of graphene platelet reinforced nanocomposite lattice sandwich plates subjected to supersonic flow, Aerosp. Sci. Technol. 138 (2023).
[32] Z. Shi, Y.F. Zhong, F. Yang, J. You, Static analysis of corrugated lattice-core sandwich panels using VAM-based model, Int J. Mech. Sci. 238 (2023).
[33] C. Li, H.S. Shen, H. Wang, Z.F. Yu, Large amplitude vibration of sandwich plates with functionally graded auxetic 3D lattice core, Int J. Mech. Sci. 174 (2020).
[34] D. Li, R.C. Gao, L. Dong, W.K. Lam, F.P. Zhang, A novel 3D re-entrant unit cell structure with negative Poisson's ratio and tunable stiffness, Smart Mater. Struct. 29 (2020).
[35] W.Y. Xu, L. Zhang, B.Q. Zhang, H.Y. Zhang, Z. Liu, P. Zhu, Crushing behavior of contact-aided AlSi10Mg sandwich structure based on chiral mechanical metamaterials, Int J. Mech. Sci. 260 (2023).
[36] J.Q. Qi, C. Li, Y. Tie, Y.P. Zheng, Y.C. Duan, Energy absorption characteristics of origami-inspired honeycomb sandwich structures under low-velocity impact loading, Mater. Des. 207 (2021).
[37] L.M. Fonseca, G.V. Rodrigues, M.A. Savi, An overview of the mechanical description of origami-inspired systems and structures, Int J. Mech. Sci. 223 (2022).
[38] M. Klaus, H.G. Reimerdes, N.K. Gupta, Experimental and numerical investigations of residual strength after impact of sandwich panels, Int J. Impact Eng. 44 (2012) 50–58.
[39] X. Zhang, X.D. Huang, G.X. Lu, Tunable bandgaps and acoustic characteristics of perforated Miura-ori phononic structures, Int J. Mech. Sci. 253 (2023).
[40] S.N. Lyu, B. Qin, H.C. Deng, X.L. Ding, Origami-based cellular mechanical metamaterials with tunable Poisson's ratio: Construction and analysis, Int J. Mech. Sci. (212 () (2021).
[41] K. Liu, G.H. Paulino, Nonlinear mechanics of non-rigid origami: an efficient computational approach, P R. Soc. a-Math. Phy 473 (2017).
[42] E.T. Filipov, K. Liu, T. Tachi, M. Schenk, G.H. Paulino, Bar and hinge models for scalable analysis of origami, Int J. Solids Struct. 124 (2017) 26–45.
[43] T.H. Zhang, K. Kawaguchi, M. Wu, A folding analysis method for origami based on the frame with kinematic indeterminacy, Int J. Mech. Sci. 146 (2018) 234–248.
[44] P.P. Pratapa, K. Liu, G.H. Paulino, Geometric Mechanics of Origami Patterns Exhibiting Poisson's Ratio Switch by Breaking Mountain and Valley Assignment, Phys. Rev. Lett. 122 (2019).
[45] K. Liu, P.P. Pratapa, D. Misseroni, T. Tachi, G.H. Paulino, Triclinic Metamaterials by Tristable Origami with Reprogrammable Frustration, Adv. Mater. 34 (2022).
[46] K. Liu, L.S. Novelino, P. Gardoni, G.H. Paulino, Big influence of small random imperfections in origami-based metamaterials, P R. Soc. a-Math. Phy 476 (2020).
[47] X.X. Dang, L. Lu, H.L. Duan, J.X. Wang, Deployment kinematics of axisymmetric Miura origami: Unit cells, tessellations, and stacked metamaterials, Int J. Mech. Sci. 232 (2022).
[48] J. Song, Y. Chen, G.X. Lu, Axial crushing of thin-walled structures with origami patterns, Thin Wall Struct. 54 (2012) 65–71.
[49] J.Y. Ma, Z. You, Energy Absorption of Thin-Walled Square Tubes With a Prefolded Origami Pattern-Part I: Geometry and Numerical Simulation, J. Appl. Mech. -T Asme 81 (2014).
[50] C.H. Zhou, B. Wang, J.Y. Ma, Z. You, Dynamic axial crushing of origami crash boxes, Int J. Mech. Sci. 118 (2016) 1–12.
[51] B. Wang, C.H. Zhou, The imperfection-sensitivity of origami crash boxes, Int J. Mech. Sci. 121 (2017) 58–66.
[52] J.Y. Ma, D.G. Hou, Y. Chen, Z. You, Quasi-static axial crushing of thin-walled tubes with a kite-shape rigid origami pattern: Numerical simulation, Thin Wall Struct. 100 (2016) 38–47.
[53] C.H. Zhou, Y. Zhou, B. Wang, Crashworthiness design for trapezoid origami crash boxes, Thin Wall Struct. 117 (2017) 257–267.
[54] K. Yang, S.Q. Xu, J.H. Shen, S.W. Zhou, Y.M. Xie, Energy absorption of thin-walled tubes with pre-folded origami patterns: Numerical simulation and experimental verification, Thin Wall Struct. 103 (2016) 33–44.
[55] M.Q. Wan, K.Q. Yu, J.P. Gu, H. Zeng, H.Y. Sun, A.A. Khatibi, 4D printed TMP origami metamaterials with programmable mechanical properties, Int J. Mech. Sci. 250 (2023).
[56] K. Chittineni, E. Woldesenbet, Characterization of Integrated Functionally Gradient Syntactic Foams, J. Eng. Mater. -T Asme 132 (2010).
[57] M. Schenk, S.D. Guest, Geometry of Miura-folded metamaterials, P Natl. Acad. Sci. USA 110 (2013) 3276–3281.
[58] J.J. Zhang, D. Karagiozova, Z. You, Y. Chen, G.X. Lu, Quasi-static large deformation compressive behaviour of origami-based metamaterials, Int J. Mech. Sci. 153 (2019) 194–207.
[59] S.C. Liu, G.X. Lu, Y. Chen, Y.W. Leong, Deformation of the Miura-ori patterned sheet, Int J. Mech. Sci. 99 (2015) 130–142.
[60] Y. Zhou, Y.T. Zhang, J. Feng, J.G. Cai, Numerical study of the hysteretic behavior of energy dissipation braces based on Miura origami, Int J. Nonlin Mech. 157 (2023).
[61] R.K. Fathers, J.M. Gattas, Z. You, Quasi-static crushing of eggbox, cube, and modified cube foldcore sandwich structures, Int J. Mech. Sci. 101 (2015) 421–428.
[62] X.Y. Zhang, S.H. Wang, Y. Durandet, S. Palanisamy, G.X. Lu, Energy absorption behavior of origami bellows under tension, Int J. Mech. Sci. 246 (2023).
[63] X. Zhou, H. Wang, Z. You, Mechanical properties of Miura-based folded cores under quasi-static loads, Thin Wall Struct. 82 (2014) 296–310.
[64] Y. Lv, Y. Zhang, N. Gong, Z.X. Li, G.X. Lu, X.M. Xiang, On the out-of-plane compression of a Miura-ori patterned sheet, Int J. Mech. Sci. 161 (2019).
[65] Z. Shi, Y.F. Zhong, X.Q. Liu, J. Shi, A VAM-based reduced-order model for M-shaped folded core sandwich plates, Int J. Mech. Sci. 231 (2022).
[66] J.M. Gattas, Z. You, Quasi-static impact of indented foldcores, Int J. Impact Eng. 73 (2014) 15–29.
[67] J.Y. Ma, J.C. Song, Y. Chen, An origami-inspired structure with graded stiffness, Int J. Mech. Sci. 136 (2018) 134–142.
[68] Z.J. Li, Q.S. Yang, R. Fang, W.S. Chen, H. Hao, Origami metamaterial with two-stage programmable compressive strength under quasi-static loading, Int J. Mech. Sci. 189 (2021).
[69] T. Wierzbicki, W. Abramowicz, On the Crushing Mechanics of Thin-Walled Structures, J. Appl. Mech. -T Asme 50 (1983) 727–734.
[70] T. Wierzbicki, Crushing analysis of metal honeycombs, Int J. Impact Eng. 1 (1983) 157–174.
[71] W.G. Chen, T. Wierzbicki, Relative merits of single-cell, multi-cell and foam-filled thin-walled structures in energy absorption, Thin Wall Struct. 39 (2001) 287–306.
[72] W. Zhang, T.X. Yu, J. Xu, Uncover the underlying mechanisms of topology and structural hierarchy in energy absorption performances of bamboo-inspired tubular honeycomb, Extrem. Mech. Lett. 52 (2022).
[73] J. Cheng, Y. Li, Foldcore structures with origami initiators for energy-absorbing sandwich panels, Acta Mech. Solid. Sin. 36 (2023) 491–505.